APPLIED PHYSICS

Ultrasound matrix imaging for 3D transcranial in vivo localization microscopy

Flavien Bureau[1]†, Louise Denis[2]†, Antoine Coudert[2], Mathias Fink[1], Olivier Couture[2], Alexandre Aubry[1]*

Transcranial ultrasound imaging is usually limited by skull-induced attenuation and high-order aberrations. By using contrast agents such as microbubbles in combination with ultrafast imaging, not only can the signal-to-noise ratio be improved, but super-resolution images down to the micrometer scale of the brain vessels can also be obtained. However, ultrasound localization microscopy (ULM) remains affected by wavefront distortions that limit the microbubble detection rate and hamper their localization. In this work, we show how ultrasound matrix imaging, which relies on the prior recording of the reflection matrix, can provide a solution to these fundamental issues. As an experimental proof of concept, an in vivo reconstruction of deep brain microvessels is performed on three anesthetized sheep. The compensation of wave distortions is shown to markedly enhance the contrast and resolution of ULM. This experimental study thus opens up promising perspectives for a transcranial and nonionizing observation of human cerebral microvascular pathologies, such as stroke.

INTRODUCTION

Transcranial imaging is essential to understand the complex vascular mechanisms underlying pathologies. For cerebrovascular events, such as strokes, x-rays and computed tomography (CT) are currently used to observe hemorrhagic events (*1*), and magnetic resonance imaging (MRI) is used to diagnose and date ischemic stroke (*2*). Although these methods allow visualization of many neurovascular diseases, MRI or CT scans require large and expensive equipment that is only primarily available in health care centers.

Alternatively, transcranial ultrasound is used in Doppler mode to monitor reperfusion after a stroke (*3*). This technique allows portable real-time imaging at low cost. However, it remains a major challenge as the complexity of the skull layer with its unpredictable porosity causes severe attenuation, strong aberrations, and multiple scattering, leading to a marked reduction in resolution and contrast of the ultrasound image.

Microbubbles are often used to improve the visualization of blood flow in ultrasound imaging (*4*–*6*). In the clinic, they are injected intravenously and are excellent contrast agents due to their high impedance mismatch compared to soft tissues. The use of ultrafast ultrasound scanners, i.e., with high frame rates, has also enabled organ perfusion dynamics to be studied with greater precision (*7*, *8*).

In addition to enhancing the blood signal, microbubbles can also be used to generate superresolved images. This is the principle of ultrasound localization microscopy (ULM) (*9*–*12*), which is based on a similar idea developed a few years earlier in fluorescence microscopy (*13*, *14*). By separating the echoes of individual injectable microbubbles, their position can be localized with subwavelength precision and tracked over time. This allows an accuracy that no longer depends on the diffraction limit but on the accuracy of detection of their center. As a consequence, ULM results in a substantial improvement in resolution by a factor of 10 (*15*) compared to standard ultrasound images. ULM has already proved its worth in many organs in depth, both preclinically (*9*, *16*–*23*) and clinically (*24*–*32*). The real-time information contained in the displacement of microbubbles enables complex vascular networks to be mapped at the micrometer scale, even going as far as the capillary-level reconstruction of functional units, such as glomeruli in the kidney (sensing ULM) (*27*–*29*). ULM imaging has even been successfully used in transcranial clinical imaging of the adult human brain (*26*), where aberration correction is critical (*33*, *34*).

Recently, three-dimensional (3D) ULM (*19*, *35*–*44*) has overcome many 2D limitations, such as the projection of 3D structures in 2D, suboptimal tracking of microbubbles, and out-of-plane probe movements that prevent vascular reconstruction. Nevertheless, aberrations caused by the skull remain a problem for ULM, especially in 3D. The sensitivity of bubble detection is lower, which affects not only the contrast of the superresolved image but also the accuracy of bubble localization, where the high sidelobes of a degraded point spread function (PSF) can cause artifacts such as vessel doubling (*34*, *45*).

To solve the fundamental problem of aberrations, adaptive focusing was introduced years ago in astronomy to compensate for phase distortions undergone by starlight when it passes through the atmosphere (*46*–*49*). This idea was then transposed to ultrasound imaging by tailoring a focusing law that either optimizes image metrics (*50*, *51*) or maximizes the spatial correlations of backscattered echoes (*52*–*56*). In the specific case of ULM, several methods have been proposed to correct the aberrations caused by the skull. A first strategy (*45*) is based on deep learning algorithms trained with numerical simulations. Although it gives impressive in vivo results for small animals, it is hampered by the specificity of the training set, so its transfer to other experimental configurations [probe, organ, and signal-to-noise ratio (SNR)] may require tedious training procedures. The second method (*34*) uses microbubbles as ultrasound guide stars but suffers several drawbacks. On one hand, microbubbles should be detected and isolated enough, which can be extremely difficult to assess because of the strongly distorted focal spot across the skull. On the other hand, the number of detected microbubbles should be large enough for self-averaging in each isoplanatic patch. Last, the demonstration was limited to 2D imaging using a 1D-phased array probe, while skull heterogeneities are 3D distributed

[1]PSL University, ESPCI Paris, CNRS, Institut Langevin, Paris, France. [2]Sorbonne Université, CNRS, INSERM, Laboratoire d'Imagerie Biomedicale, Paris, France.
*Corresponding author. Email: alexandre.aubry@espci.fr
†These authors contributed equally to this work.

and require a bidimensional control of the ultrasonic wave field to properly compensate for these high-order aberrations (*57*).

Inspired by previous seminal works (*58*–*60*), a matrix approach of ultrasound imaging has been recently developed to overcome aberrations without any guide star (*61*, *62*). On the basis of the recording of the reflection matrix associated with the ultrasonic probe and the linearity of the wave equation, it allows the simulation of wave focusing in postprocessing and an iteration of this process toward local adaptive focusing laws in ultrasonic speckle (*63*). An optimized contrast and close-to-ideal resolution are then obtained for each voxel of the ultrasound image. Ultrasound matrix imaging (UMI) has been successfully applied to transcranial 3D imaging of a head phantom (*57*).

The goal of this paper is to demonstrate the interest in UMI for in vivo 3D brain imaging. In particular, we will show how (i) UMI can be used to quantify aberrations and multiple scattering in in vivo transcranial imaging, (ii) UMI can exploit static speckle from brain tissue to tailor complex 2D focusing laws in a strong aberration and multiple scattering regime, (iii) ULM can leverage these focusing laws despite motion to increase the detection rate of microbubbles and improve their localization, and (iv) UMI can be combined to ULM to provide a 3D, artifact-free, superresolved, and contrasted image of brain vessels.

To that aim, an experimental proof of concept will consist of brain imaging on three anesthetized sheep. The first step of the experimental procedure consists in the acquisition of the reflection matrix and the estimation of local focusing laws by means of UMI. The second step consists in a microbubble injection and the beamforming of ultrafast images using the focusing laws provided by UMI. The last part consists in the usual ULM postprocessing that comprises localizing and tracking microbubbles. Final ULM image contrast will be shown to be markedly improved by the better detection rate of smaller micrometer-sized vessels provided by UMI. The comparison with MRI will show how UMI allows the removal of artifacts from which the initial ULM image suffered.

RESULTS

Reflection matrix in a virtual source basis

Here, we demonstrate transcranial brain imaging by overcoming the major challenges of (i) skull bone aberration with 3D UMI and (ii) diffraction-limited resolution with the super-resolution feature provided by ULM. As a proof of concept, the same experimental protocol (Fig. 1) has been applied to three anesthetized sheep (see Materials and Methods). A 32×32 array of transducers is placed on the shaved head of each sheep directly over the crest of the frontal bone (Fig. 1B). The probe is driven in a 1- to 2-MHz frequency bandwidth to limit the attenuation by skull bone (*64*). The first ultrasound sequence consists of recording a high-dimensional reflection matrix $\mathbf{R}_{uv}(\tau)$ (Fig. 1C) that contains the scattered wave field $R(\mathbf{u}_{out}, \mathbf{v}_{in}, \tau)$ recorded by each transducer $\mathbf{u}_{out}$ of the probe as a function of the echo time τ for a set of 324 incident diverging waves. This illumination basis is associated with a set of virtual transducers $\mathbf{v}_{in}$ placed behind the probe (see Materials and Methods and fig. S1). It maximizes the SNR across the targeted field of view (*65*). The number of incident waves is dictated by our choice of the maximal angular range spanning from −30° to +30° (see Materials and Methods).

Quantifying skull-induced aberrations and scattering

In contrast with standard beamforming that relies on the principle of confocal imaging, the cornerstone of UMI consists in decoupling the input and output focal spots in postprocessing. Mathematically, such a beamforming procedure can be written as follows

$$R(\boldsymbol{\rho}_{out}, \boldsymbol{\rho}_{in}, z) = \sum_{\mathbf{v}_{in}} \sum_{\mathbf{u}_{out}} R(\mathbf{u}_{out}, \mathbf{v}_{in}, \tau_{in}(\mathbf{v}_{in}, \boldsymbol{\rho}_{in}, z) + \tau_{out}(\mathbf{u}_{out}, \boldsymbol{\rho}_{out}, z)) \quad (1)$$

where $\mathbf{r}_{in} = (\boldsymbol{\rho}_{in}, z)$ and $\mathbf{r}_{out} = (\boldsymbol{\rho}_{out}, z)$ are the coordinates of the input and output focal points, respectively. τ_{in} and τ_{out} are the expected travel times for the wave to go from the source/detector to the input/output focusing point (see Materials and Methods and Eq. 4). The result of Eq. 1 is a focused reflection matrix $\mathbf{R}_{\boldsymbol{\rho}\boldsymbol{\rho}}(z)$ whose coefficients $R(\boldsymbol{\rho}_{out}, \boldsymbol{\rho}_{in}, z)$ probe the cross-talk between a virtual source and detector at lateral positions $\boldsymbol{\rho}_{in}$ and $\boldsymbol{\rho}_{out}$, respectively, both located at the same depth z inside the medium (Fig. 2A). This matrix enables a local quantification of the focusing quality and multiple scattering by providing a local PSF in reflection (RPSF) (*57*, *62*, *66*) (see Materials and Methods and Eq. 7). Figure 3B display maps of RPSFs at depth $z = 35$ mm for each sheep. In the single scattering regime and in the absence of aberrations, the RPSF would exhibit a confocal diffraction-limited peak. On the contrary, the various

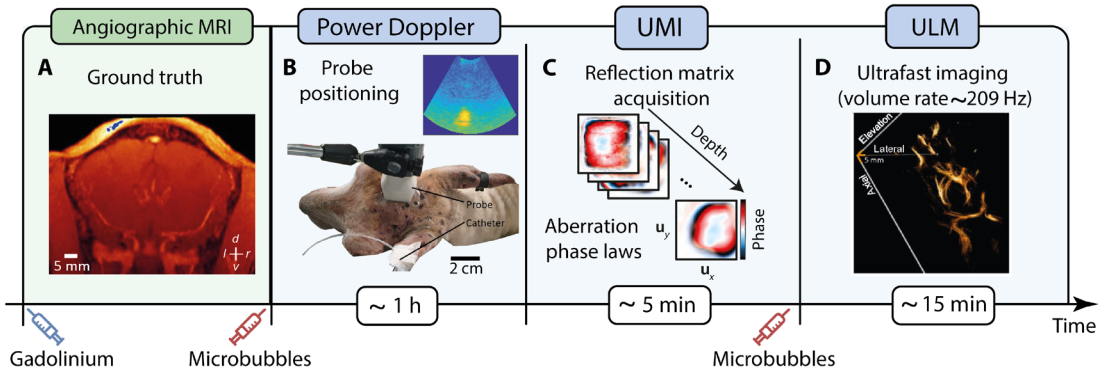

Fig. 1. Sheep experiment: A multisequence acquisition. (**A**) Angiographic MRI. (**B**) Transcranial power Doppler for positioning the probe. (**C**) Acquisition of the reflection matrix to estimate local aberration laws with 3D UMI. (**D**) Ultrafast imaging for superresolved ULM images. The images shown in this figure are for illustrative purposes only and do not provide quantitative results. h, hours; min, minutes; l, left; d, dorsal; v, ventral; r, right.

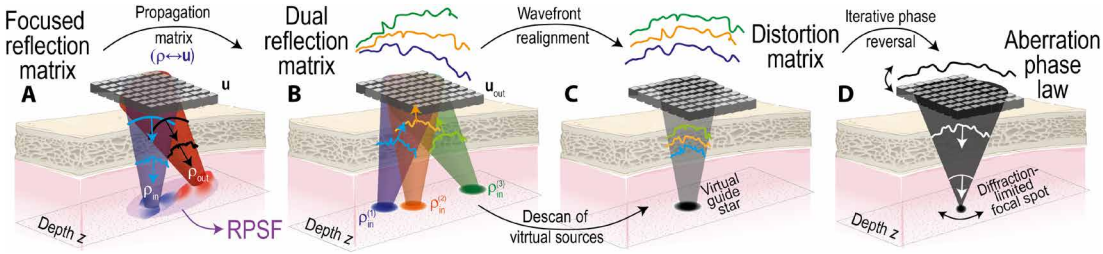

Fig. 2. Principle of UMI. (**A**) Focused reflection matrix contains the time-gated response between virtual source ($\boldsymbol{\rho}_{in}$) and detector ($\boldsymbol{\rho}_{out}$) located at the same depth *z*. (**B**) An output projection of the focused reflection matrix in the transducer basis ($\mathbf{u}_{out}$) provides the reflected wavefronts induced by each virtual source ($\boldsymbol{\rho}_{in}$) at depth *z*. (**C**) Those wavefronts are realigned to extract the wavefront distortions induced by the mismatch between the real speed-of-sound distribution and the wave velocity model. Seen from the focused basis, this operation leads to an angular descan of each virtual source at the same position, leading to the synthesis of a virtual guide star. (**D**) Exploiting the correlations between each distorted wavefront, an iterative phase reversal (IPR) algorithm extracts an aberration phase law that can be used to compensate for wave distortions induced by the skull and, ideally, retrieve a diffraction-limited focal spot across the field of view.

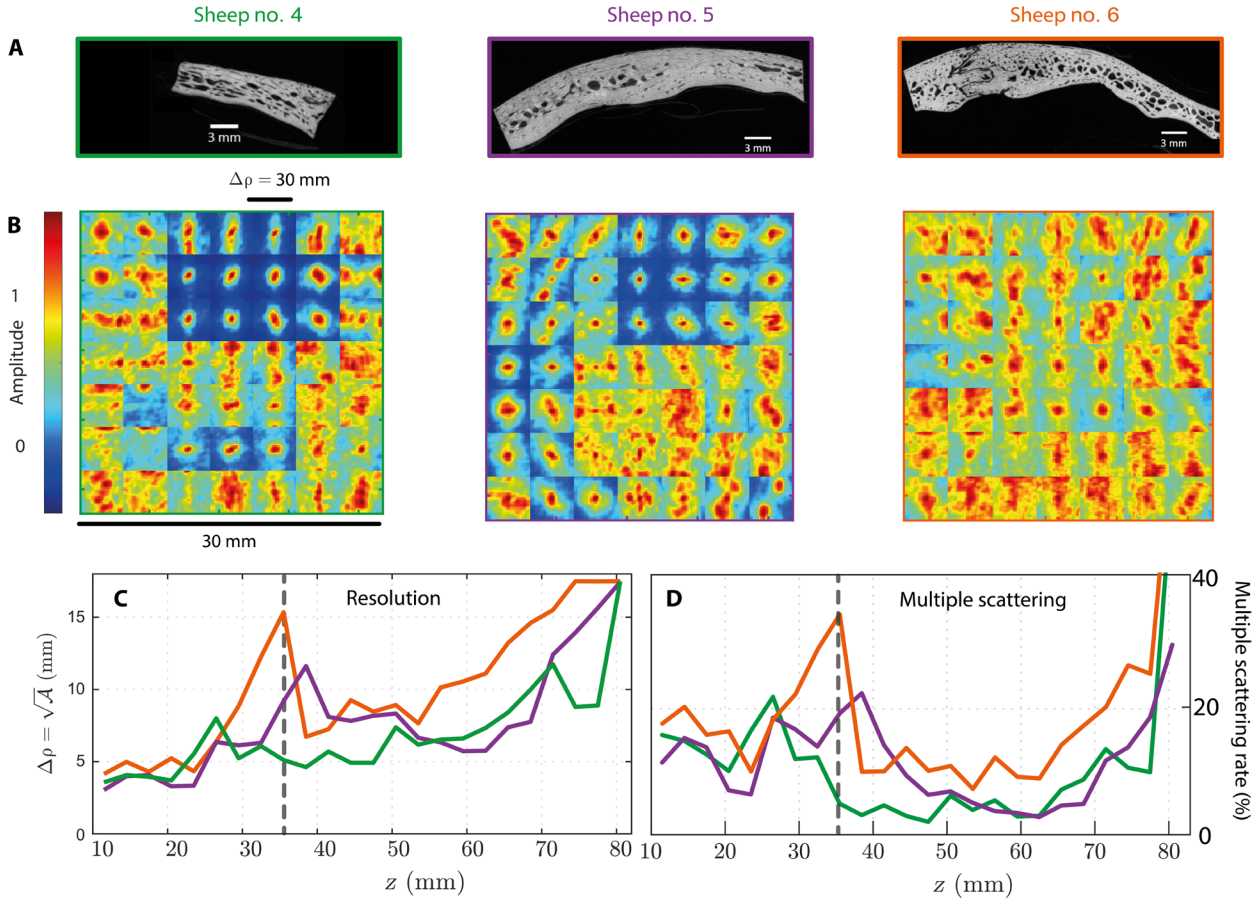

Fig. 3. Influence of cranial heterogeneities on aberration and multiple scattering. (**A**) Micro-CT of each sheep skull. Left, sheep no. 4; middle, sheep no. 5; right, sheep no. 6. (**B**) Corresponding RPSF maps at depth $z = 35$ mm. (**C** and **D**) RPSF extension and multiple scattering rate as a function of depth, extracted by UMI, for sheep no. 4 (green line), no. 5 (purple line), and no. 6 (orange line).

RPSFs here display a distorted focal spot induced by wave velocity heterogeneities on top of an incoherent background due to multiple scattering events induced by the skull. Notably, whatever the imaging depth is, the RPSF looks more distorted and less contrasted for sheep no. 6 than for sheep no. 4 and no. 5 (Fig. 3B).

On one hand, the aberration level can be quantified by investigating the spatial extent δρ of the RPSF (fig. S4) (*61*, *63*). The depth evolution of δρ is shown in Fig. 3C. The general trend is not only a degradation of the resolution with depth, as predicted by diffraction theory, but also a more important aberration level in sheep no. 6. This difference of behavior can be understood by looking at the micro-CT of each skull (Fig. 3A). While the skulls of sheep no. 4 and no. 5 show a regular thickness ($L \sim 4.2 \pm 1.1$ mm and $L \sim 5.3 \pm 1$ mm, respectively), skull no. 6 displays a more irregular shape:

$L \sim 5.7 \pm 1.7$ mm (*42*). This difference of morphology between the three skulls could explain the higher degree of aberrations observed in sheep no. 6.

On the other hand, the multiple scattering rate can be estimated from the incoherent background of the RPSF (see Materials and Methods and Eq. 9). It appears that the multiple scattering rate is far from being negligible even after the beamforming process, since it reaches a value of 30% in the $z = 35$-mm region for sheep no. 6 (Fig. 3D). As with the aberration level, the multiple scattering rate is larger for this sheep over almost the whole depth range. This feature can be understood by looking at the internal structure of the bone. The diploë volume ratio ν is much higher in sheep no. 6 ($\nu = 57\%$) than in sheep no. 4 and no. 5 ($\nu = 14\%$ and $\nu = 29\%$, respectively) (*42*). This high degree of heterogeneity seems to account for the higher multiple scattering rate observed in sheep no. 6.

Overcoming wave distortions

The complex speed-of-sound distribution highlighted in Fig. 3B hampers ultrasound brain imaging. The confocal image of the brain, which can be extracted from the diagonal coefficients of $\mathbf{R}_{\boldsymbol{\rho\rho}}(z)$ (see Materials and Methods and Eq. 5), is blurred by the skull heterogeneities (Fig. 4A). Fortunately, an optimized contrast and diffraction-limited resolution can be recovered using the distortion matrix concept (*57*, *62*, *66*). This matrix contains the wave distortions exhibited by each reflected wavefront in the transducer basis (Fig. 2C). The choice of this basis is dictated by the fact that most aberrations are induced by the skull heterogeneities, i.e., in the vicinity of the probe. An iterative phase reversal (IPR) process is then applied to the distortion matrix to provide an estimation of an aberration phase law, $\phi(\mathbf{u}_{\text{out}}, z)$, at each depth (see Materials and Methods, Fig. 2D, and movie S1). Examples of aberration phase laws are displayed in Fig. 4C. They show a complex feature, as quantified by the Strehl ratio $\mathcal{S}$ that provides the ratio between the energy at focus with and without aberrations (*67*) (see Materials and Methods and Eq. 18). For instance, the aberration law measured at depth $z = 50$ mm exhibits a Strehl ratio $\mathcal{S} = 0.03$. This extremely low value illustrates the detrimental impact of skull heterogeneities on the focusing process. A more detailed quantification of the aberration magnitude is provided in section S3 by evaluating the modulus of the aberration transfer function. As expected from the previous RPSF analysis (Fig. 3), the aberration magnitude is found to be 30% larger in sheep no. 6 compared to sheep no. 4 and no. 5.

The aberration phase laws can be leveraged to compensate for the wave distortions exhibited by the focused reflection matrix (see Materials and Methods). The resulting confocal image is displayed in Fig. 4E. It exhibits a clear improvement compared to the initial confocal image (Fig. 4A), with a contrast gain of 8 dB for the deepest bright scatterers ($z = 50$ and 60 mm). The efficiency of the correction process can be assessed by comparing the maps of RPSFs before (Fig. 4B) and after (Fig. 4D) aberration compensation. The spatial resolution is improved by a factor between 2 and 3, and the multiple scattering background is decreased by more than 10 dB beyond $z = 50$ mm (fig. S5). Nevertheless, the obtained RPSFs remain imperfect in Fig. 4D. High-order aberrations subsist because of their anisoplanicity. Last, although the confocal image shows a clear improvement, the diffraction-limited resolution $\delta\rho_0$ remains limited by the probe size D: $\delta\rho_0 \sim \lambda z/D$.

Matrix imaging for ULM

To overcome diffraction, we then perform ULM by injecting boluses of microbubbles and tracking them using an ultrafast imaging sequence (see Materials and Methods). To that aim, we use a hybrid transmit basis with three cylindrical waves emitted by the entire probe and two spherical diverging waves transmitted successively by each probe panel (*68*). This sparse emission basis, referred to as $\mathbf{s}_{\text{in}}$, yields a volume rate of 209 Hz (see Materials and Methods). For each incident wave field, the raw data are stored in a set of new reflection matrices $\mathbf{R}'_{\mathbf{us}}(\tau, t_m) = [R'(\mathbf{u}_{\text{out}}, \mathbf{s}_{\text{in}}, \tau, t_m)]$ recorded at different times t_m. A set of 3D images is then obtained by beamforming

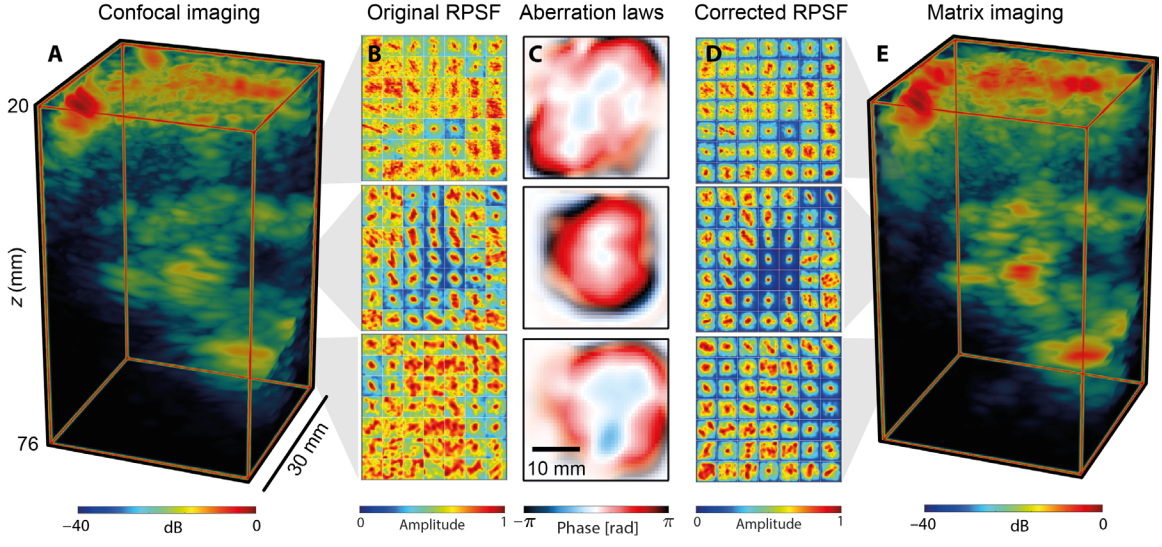

Fig. 4. UMI in the sheep brain. (**A**) Confocal volume extracted from the diagonal of the focused **R**-matrices (see Materials and Methods and Eq. 5). (**B** to **D**) Maps of initial RPSFs, aberration phase laws, and corrected RPSFs, respectively, at three different depths $z = 32$ mm (top), $z = 50$ mm (middle), and $z = 68$ mm (bottom). Each RPSF is displayed in a scan range $\Delta\boldsymbol{\rho} = \boldsymbol{\rho}_{\text{out}} - \boldsymbol{\rho}_{\text{in}}$ (see Materials and Methods) that varies from −15 to +15 mm in both *x* and *y* directions. (**E**) Confocal volume after aberration correction. The results shown here correspond to ultrasound data acquired on sheep no. 6.

the reflection matrix rephased by the conjugate of the aberration law to compensate for skull-induced aberrations

$$\mathcal{I}'(\mathbf{r},t_m)=\sum_{\mathbf{s}_{in}}\sum_{\mathbf{u}_{out}}\exp\left[-j\phi(\mathbf{u}_{out},z)\right]\times R'\left[\mathbf{u}_{out},\mathbf{s}_{in},\tau_{in}(\mathbf{s}_{in},\boldsymbol{\rho},z)+\tau_{out}(\mathbf{u}_{out},\boldsymbol{\rho},z),t_m\right] \quad (2)$$

After filtering out the static component in the image series (see Materials and Methods), the dynamic component of the brain can be highlighted. A 2D cross section of the resulting image is displayed in Fig. 5B at a given time t_m. This image is compared to its raw counterpart (Fig. 5A) obtained without aberration compensation. Because of UMI, isolated microbubbles show less distorted focal spots, as shown by two examples in the purple and red squares in Fig. 5 (A and B). Just above (~50 mm), a halo of microbubbles in the blue square seems to indicate the presence of a vessel, but the individual detection of each microbubble is complicated by their high concentration.

A deconvolution of the dynamic image with a theoretical PSF and the application of a detection threshold provide a localization of bubbles in the field of view (see Materials and Methods). The position of the detected bubbles are highlighted with red points in Fig. 5 (A and B). While several microbubbles are wrongly assigned to the high side lobes of each distorted focal spot in Fig. 5A, UMI markedly reduces this number of false detection in Fig. 5B by restoring a satisfying PSF, in particular, in the colored squares. Despite this reduction of false alarms, the number of localized microbubbles is increased. Figure 5C illustrates this assertion by showing, for sheep no. 6, the higher number of detected bubbles over time with UMI. The different peaks correspond to each injection of microbubbles.

To further reduce the false alarm rate and better appreciate the effect of UMI, we can track microbubbles over time (see Materials and Methods). In the absence of aberration correction, the focal spot is distorted, and bubbles cannot be detected on each frame during their journey across the field of view. The bubble trajectory is then subdivided into shorter tracks. As a consequence, the track length is a relevant observable to demonstrate the benefit of the aberration correction process (*34*). Figure 5D shows the increase in detected tracks provided by UMI as a function of their length. UMI notably increases the number of detected tracks by a factor ranging from 40 to 250% according to the track length. Table 1 shows the same observable for different minimum path lengths. The general trend is the same for each acquisition, thereby showing the robustness of UMI and its benefit in each imaging configuration. This result is crucial for ULM images, as the longest tracks are the most reliable for delineating small vessels.

ULM density maps are built by counting the number of tracks crossing each voxel of the field of view. These volumes are shown from two different angles in Fig. 6. The typical structure of the cerebral vessels can already be recognized before aberration correction (Fig. 6, A and C). This structure is known as the Willis circle (*69*) and can be seen as the main crossroad of the main vessels in the brain.

However, the skull heterogeneities also induce artifacts such as the duplication of one artery that can be noticed at the bottom of the conventional ULM image (Fig. 6, A and C). This type of artifact has already been observed in transcranial imaging in both mouse (*45*) and human (*34*). Notably, the focusing laws extracted by UMI (Fig. 4C) allow the removal of such artifacts as highlighted by the corrected ULM images in Fig. 6, B and D. More generally, the higher detection rate and correct repositioning of microbubbles lead to a better contrast for ULM as highlighted by the vessel network on top of the Willis circle (z = 25 to 35 mm) that appears much brighter (+6 dB) and better resolved. A similar resolution and contrast can be observed for the other 3D ULM images shown in fig. S9 and corresponding to other acquisitions on the three sheep. The impact of UMI is less marked for sheep no. 4 and no. 5 than for sheep no. 6

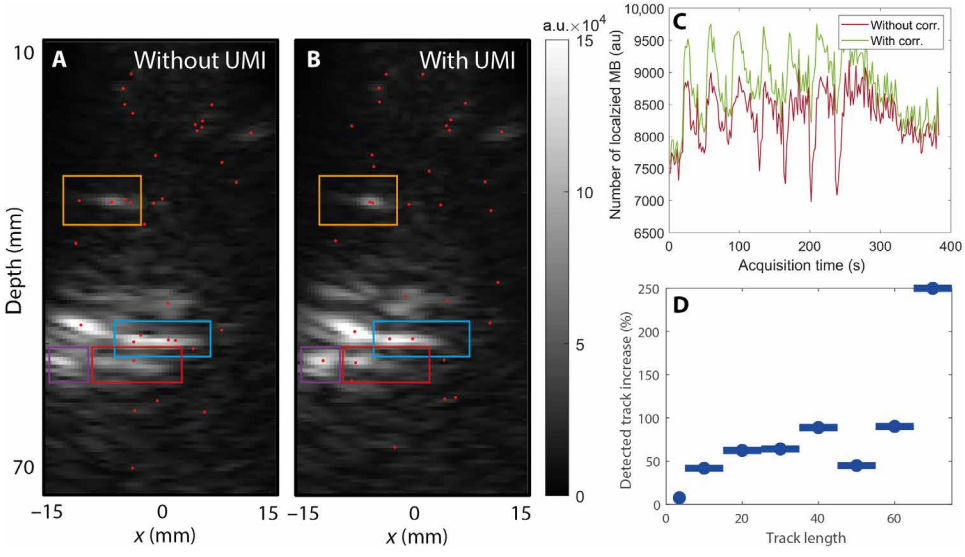

Fig. 5. Enhancing microbubble localization accuracy with UMI. (**A** and **B**) Sagittal middle slice of the ultrasound image without and with aberration correction at a given time, respectively. The position of the detected microbubbles is highlighted by red dots. The blue and orange boxes show areas where false alarms are reduced by reducing the side lobes of the PSF. The purple region shows a region where aberration compensation allows the detection of a microbubble. The red square highlights a zone where a microbubble is reassigned at a new location. (**C**) Number of localized microbubbles as a function of the acquisition time t_m with (green) and without (pink) UMI. (**D**) Increase of the microbubble detection rate with UMI for different track lengths. The data shown here correspond to sheep no. 6 (acquisition 4). a.u., arbitrary units.

Table 1. Quantification of UMI benefits on ULM tracks. Percentage of additional tracks provided by UMI for various minimal tracks length expressed in frames.

Sheep number	Acquisition number	Additional tracks detected with UMI correction (%)				
		≥2 frames	>3 frames	>5 frames	>10 frames	>30 frames
S4	1	24.0	41.7	49.1	63.3	121.7
S5	1	14.1	26.6	35.7	54.5	76.6
	2	7.5	13.7	16.2	28.5	42.8
S6	1	15.4	16.3	19.2	23.5	43.5
	2	8.7	13.3	15.3	19.1	36.1
	3	6.7	11.5	13.2	17.3	18.3
	4	6.9	22.3	32.5	47.2	66.2
	5	8.7	27.9	32.5	53.5	77.1
Mean		11.5	21.7	26.7	38.4	60.3
SD		6.0	9.0	11.2	16.1	28.5

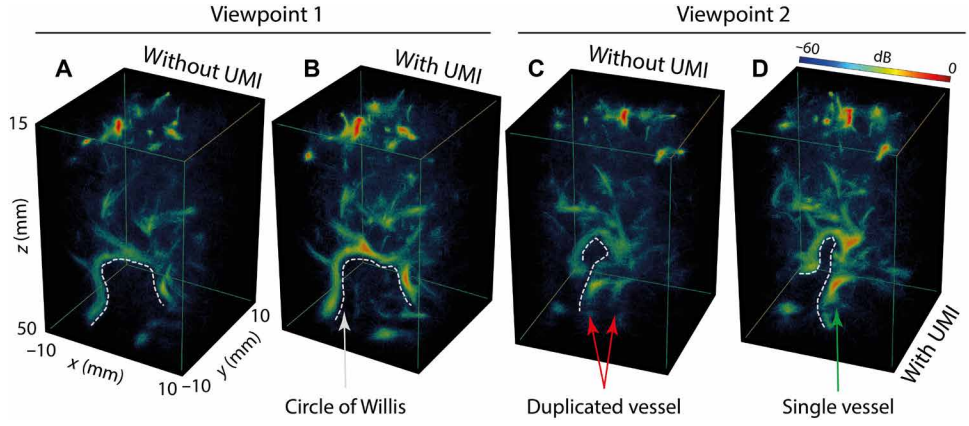

Fig. 6. Correcting ULM images with UMI. 3D images shown as maximum intensity projections from two different points of view. ULM volumes (**A** and **C**) before and (**B** and **D**) after aberration compensation. The polygon of Willis is depicted by a dashed white line and is located around $z = 40$ to 45 mm. The same dynamic range is displayed for all images. The data shown here correspond to sheep no. 6 (acquisition 4).

because the corresponding skulls generate less multiple scattering and aberration (Fig. 3). However, the aberration and scattering conditions in sheep no. 6 are the ones usually met for transcranial ultrasound imaging in humans.

To appreciate more quantitatively the benefit of UMI, we superimpose the ULM density maps on magnetic resonance angiography (MRA) sequence, which is considered as the gold standard for observing large vascular structures in the brain. After UMI, the ULM density maps match more closely with the vessels revealed by MRA. In the coronal slice (Fig. 7, A and C), UMI allows a more complete and brighter reconstruction of the vascular network (Fig. 7C) that matches in depth with the Willis polygon revealed by MRA, especially in the anterior cerebral arteries that deviate from the polygon (green and blue arrows). A zoom on the right anterior cerebral artery is displayed in fig. S8 and highlights the marked gain in contrast provided by ULM compared to MRA around the Willis circle. This benefit of UMI can be quantified by a loss of image entropy (*70*) increased by a factor of 5 with UMI.

In the sagittal section (Fig. 7, B and D), ULM provides a better adequation between MRA and ULM images of venous system (yellow arrows). This observation can be quantified by a computing structural similarity index between MRA and ULM images. This similarity metric is increased by a factor of 2 with UMI (fig. S7). Besides the repositioning of large vessels, the increase in the total SNR of the ULM volume and the appearance of small vessels provided by UMI are notable not only compared to the initial ULM image but also with respect to MRA, which only provides an image of the largest vessels (fig. S8).

Last, note that the volume rate (209 Hz) of our system limits the ability of the ULM pipeline to track microbubbles traveling in the larger cerebral vessels and to provide an appropriate flow velocity map (*26*). In the future, a 3D ultrasound scanner with a higher volume rate could alleviate this issue and provide additional physiological information.

DISCUSSION

Compared to a previous study on a static brain phantom (*57*), we have demonstrated here the benefit of UMI for transcranial in vivo imaging. Besides improving the contrast and resolution of standard

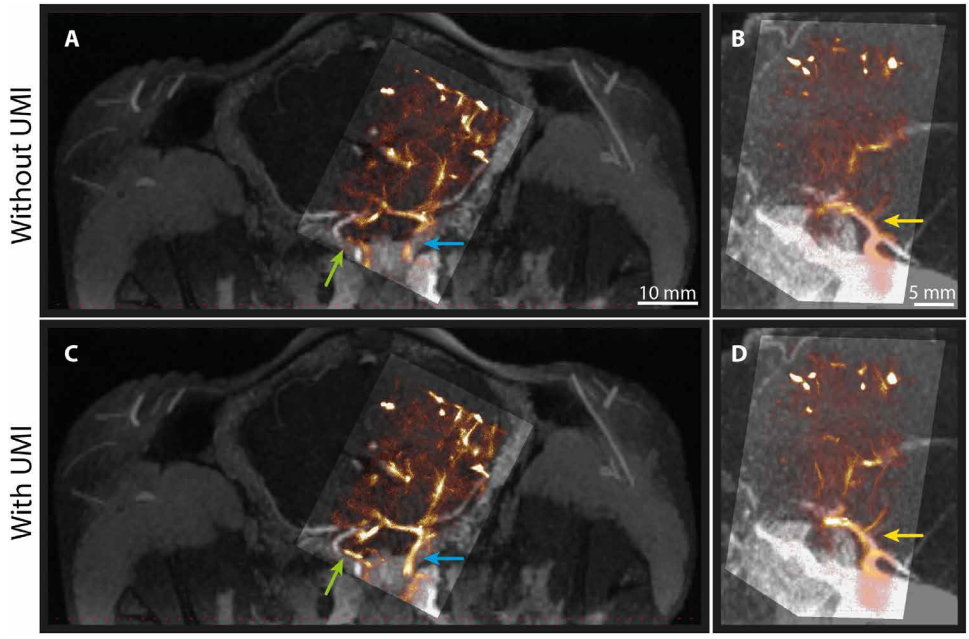

Fig. 7. Confronting ULM density maps to MRA images. (**A** and **B**) Coronal slices and sagittal slices, respectively: The ULM sections are shown as maximum intensity projections of 5-mm (coronal) and 1-cm (sagittal) thickness. Arbitrary color maps are used with fixed dynamic range for the ULM (hot color map) and MRA (black-and-white scale) images to facilitate their comparison. (**C** and **D**) Same images as in (A) and (B) with ULM images corrected by UMI. Green and blue arrows show a better reconstruction of the posterior cerebral arteries in deviation from the Willis polygon. Yellow arrows show the correction in the venous system. The data shown here correspond to sheep no. 6 (acquisition 4).

ultrasound brain images, we also showed that it can be fruitfully coupled to other imaging modalities such as ULM. While the gain in contrast provided by UMI leads to increase the overall number of detected microbubbles, it also drastically extends the length of the microbubble tracks, which is affected by SNR, point-source separability, and localization precision. Because UMI reduces the side lobes of the imaging PSF, the localization of microbubbles is actually much sharper. Doing so, UMI provides a more detailed ULM image and the removal of common artifacts such as duplication of vessels. The success of UMI has been confirmed by confronting ULM images with gold-standard MRA.

More fundamentally, UMI also showed some correlation between the aberration level and the skull thickness variations. It also highlighted the impact of diploë volume fraction on the multiple scattering level. The notable result of UMI on sheep no. 6 is promising for applications of UMI on human brain imaging, since this skull heterogeneity is in line with what is expected for human brain imaging across the temporal window (*71*, *72*).

The UMI approach for aberration compensation is perfectly complementary with the alternative route proposed recently by Robin *et al.* (*34*) that exploited bubbles as ultrasound guide stars for transcranial adaptive focusing. To some extent, UMI is more robust, since it directly synthesizes virtual guide stars from speckle (*62*) and can work whatever the concentration of bubbles is as well as in stronger aberration and under multiple scattering conditions. Typically, we were not able to apply the approach proposed in (*34*) because of the low quality of the ULM data. The latter method requires the presence of bubbles whose associated focal spot displays a correlation degree γ larger than 0.6 with the ideal diffraction-limited PSF. Here, the normalized Strehl ratio, whose value is a maximum bound for γ, ranges from 0.1 to 0.4 (section S3). Such an aberration level makes difficult the use of microbubbles as guide stars in an adaptive focusing scheme. However, in a more favorable case, static speckle and microbubbles could be a complementary source of information to enhance ULM.

In section S6, we also show how UMI provides a flexible benchmarking framework to show the benefits of the IPR process (*57*) compared with conventional aberration correction methods in speckle such as iterative time reversal (*54*) or singular value decomposition beamforming (*73*, *74*). The latter approaches actually act as an adaptive filter. While this feature is not particularly detrimental for a moderate level of aberrations, it becomes problematic in the presence of distributed attenuation, strong aberration, and multiple scattering. Unlike UMI, those alternative methods result in enlarged focal spots (fig. S6) that would lead to a lower SNR (i.e., lower bubble detection rate) and a substantial increase in bubble localization error for ULM.

Nevertheless, in the current realization, UMI also showed some limits. First, it requires the prior recording of a high-dimensional reflection matrix. Second, in the present case, it only provided the depth dependence of aberration phase laws and was not able to capture the lateral variations of aberrations. Last, it did not compensate for the multiple reverberations inside the skull that prevented us from brain imaging right below the skull. Those limits are explained by the fact that high-order aberrations and reverberations are associated with extremely small isoplanatic patches. This feature limits the efficiency of the spatial averaging process required for the synthesis of a coherent guide star in matrix imaging (Fig. 2).

In future work, these limits will be addressed by exploiting the dynamics of blood vessels. Rapid decorrelation of speckle may offer

an opportunity, as it provides numerous speckle realizations for a single voxel. Therefore, the aberration phase laws could, in principle, be extracted at a higher spatial resolution, since UMI would no longer have to rely on the isoplanicity assumption (*75*, *76*). That is, time averaging will replace spatial averaging, and the aberration phase laws can be extracted directly from the ultrafast sequence (Fig. 1D) and not from a prior static sequence (Fig. 1C). This access to a large number of disorder realizations can also be leveraged for tailoring complex spatiotemporal focusing laws capable of harnessing multiple reverberations.

In the future, we therefore expect that aberration and scattering compensation provided by UMI could help ULM in the detection and classification of cerebrovascular accidents in humans. An important goal will be to distinguish between ischemic and hemorrhagic strokes in the early phase, as has been done in the rat brain (*36*). Therefore, one perspective of this work is to conduct a pilot study with patients who have recently suffered a stroke.

Here, we have shown the great advantages and relative simplicity of the UMI and ULM combination. 3D transcranial in vivo imaging of sheep brain has been performed and shown to be in excellent agreement with gold-standard MRA. Although we have proven this claim for the specific case of ultrasound data acquired with a multiplex matrix probe, these results are much more general. UMI can be applied to any other ultrasound probe (e.g., sparse or row-column array), to any other modality (e.g., conventional Doppler or shear wave elastography), and to either 2D or 3D configurations. Beyond the specific case of ultrasound, this study paves the way toward the combination of matrix imaging (*77*, *78*) with super-resolution localization techniques (*13*) in all fields of wave physics, ranging from optical microscopy with fluorescent molecules (*79*) to seismology for dynamic imaging of glaciers (*80*, *81*).

MATERIALS AND METHODS

Experimental procedure

All experiments were performed between October 2022 and January 2023 in accordance with ARRIVE guidelines, the European Directives, and the French Legislation on Animal Experimentation (#32738) and approved by the local ethics committee (CENOMEXA no. 54). A total of six female domestic sheep were included in the study (*Ovis aries* weighing 35 to 40 kg and aged 15 to 16 months). Three of them were used to optimize the experimental protocol, and the other three are presented here (table S1).

The sheep were sedated with ketamine (12 mg/kg) and xylazine (1 mg/kg) for placement of the venous catheter. Propofol (100 μg/kg) was then administered, and endotracheal intubation was performed. During the surgical and imaging procedures, anesthesia was maintained by administration of sevoflurane (1.5 to 2.0%) in air. Cardiac activity, oximetry, and arterial pressure (between 80 and 120 mmHg) were monitored throughout the procedure. Respiratory rate and tidal volume were adjusted to maintain physiologic limits, and body temperature was maintained at 38°C with a warming blanket.

At the end of the ultrasound examination, i.e., after 5 hours, the anesthesia was terminated so that the animal could wake up and be returned to its box. Three imaging sessions were performed within 1 to 2 weeks. At the end of the last imaging session, the sheep was euthanized with a barbiturate overdose (pentobarbital, 0.2 g/kg) after 2 min of 8% sevoflurane inhalation. A controlled arterial pressure of less than 20 mmHg and no cardiac activity were used to assess death.

After the last imaging session and the death of the animal, the part of the skull below the probe was removed for cleaning and preserved in saline and bleach. This subject was then fixed in a bath of formalin-free fixative F13 (Morphisto, Germany) for 1 day and then dried and placed under vacuum for micro-CT imaging (Skyscan 1176, Bruker, Kontich, Belgium; voxel size, 18 μm) (*42*).

Ultrasound sequences

A low-frequency matrix array probe (Vermon, Tours, France), as described in Table 2, is placed on the shaved head of the sheep directly over the crest of the frontal bone. 3D ultrasound sequences were then recorded with a Vantage 256 4-to-1 multiplex system [Verasonics Universal Transducer Adapter (UTA) 1024-MUX adapter, Kirkland, USA]. The 1024 elements were connected to the 256 channels of the ultrasound scanner using a 4-to-1 multiplexer (Verasonics UTA 1024-MUX adapter). The probe is therefore divided into four panels, the multiplexer only allowing emission with one panel and receiving with another (*42*, *68*). For the reflection matrix acquisition, a set of 16 emissions had to be performed for any incident wave field to record the 4 × 4 responses between each panel at emission and reception. Those recordings are then reassembled in postprocessing to get the full reflected wavefront associated with each synthetic incident wave field. For the ULM sequence, this constraint has been partially mitigated, since it is possible to emit with the four connected panels at the same time, provided that the emission waveform and delays were identical along the elevation axis (*42*, *68*). As detailed further, the incident cylindrical wavefronts were therefore used to reach a sufficient frame rate for ULM. The successive ultrasound imaging sequences of the entire sheep experiment are summarized in Fig. 1.

Table 2. Matrix array datasheet.

Number of transducers	32 × 32 = 1024 (with five dead elements)
Geometry (*y* axis)	Three inactive rows between each block of 32 × 8 elements
Pitch	$\delta u = 0.55$ mm ($\approx\lambda/2$ at $c = 1540$ m/s)
Aperture	$\Delta\mathbf{u} = \begin{pmatrix} \Delta u_x \\ \Delta u_y \end{pmatrix} = \begin{pmatrix} 17.6\text{mm} \\ 19.3\text{mm} \end{pmatrix}$
Central frequency	$f_c = 1.56$ MHz
Bandwidth	60% → [1–2] MHz
Transducer directivity	$\theta_{max} = 64°$ at $c = 1540$ m/s

Initial real-time power Doppler imaging is used to correctly position the probe before acquiring longer ultrasound data. This sequence is performed with the injection of microbubble contrast agent (SonoVue, Bracco, Italy) (*82*) to obtain SNR-enhanced images of the cerebral vasculature. Once a sufficiently good signal is obtained, the probe is fixed, and we wait until the microbubbles have disappeared, i.e., 10 min.

A UMI sequence is then performed. It consists of the acquisition of the reflection matrix using a set of 324 synthetic spherical waves whose associated virtual sources are located along a sphere radius $\mathcal{R} = 39.5$ mm: $\mathbf{R}_{\mathbf{uv}}(t) = \left[R\left(\mathbf{u}_{\text{out}}, \mathbf{v}_{\text{in}}, t\right)\right]$, where the vector $\mathbf{v}_{\text{in}}$ indicates the position of the corresponding virtual sources (see fig. S1) and $\mathbf{u}_{\text{out}}$ refers to the position of the transducers. The insonification of the medium is made with diverging waves associated with virtual sources located above the probe (*65*), such that

$$\mathbf{v} = \begin{pmatrix} v_x \\ v_y \\ v_z \end{pmatrix} = -\mathcal{R}\begin{pmatrix} \sin\theta_x \\ \sin\theta_x \\ \sqrt{1-\sin^2\theta_x - \sin^2\theta_y} \end{pmatrix} \tag{3}$$

with $\boldsymbol{\theta} = \left(\theta_x, \theta_y\right)$ as the angle associated with each virtual source. The angular range spans from $-\sin\theta_{\text{m}}$ to $+\sin\theta_{\text{m}}$, with $\theta_{\text{m}} = 30^{\text{o}}$. The angular pitch $\delta(\sin\theta)$ is governed by the probe extension $\delta(\sin\theta) = \lambda_{\text{c}} / \Delta u$, with $\lambda_{\text{c}} = c_0 / f_{\text{c}}$, the central wave length. This angular range and angular pitch dictate the number of incident diverging waves $N = \left[2\sin\theta_{\text{m}} / \delta(\sin\theta)\right]^2 \sim 324$.

Last, a hybrid ULM sequence is performed. To limit the number of incident waves, only the azimuth and elevation shifts (θ_x,θ_y) of (0, 0), (−5, 0), (5, 0), (0, −5), and (0, 5) degrees are considered. As stated above, the 4-to-1 multiplexer imposes a sequence of 16 insonifications to record the response of the medium for each virtual source. Such a sequence is prohibitive for high-frame rate imaging. However, this condition can be relaxed by only recording the responses between neighboring panels, thereby restricting the number of insonifications to 10 for each virtual source (*68*). Moreover, the four panels can be connected together for the emission if the delays are similar in the elevation direction. For such an incident cylindrical wavefront, only four successive transmissions are required for the four reception apertures. However, full cylindrical waves could only be induced when the angle θ_x is 0 in the azimuthal direction. In the *y* direction, waves still needed to be split in multiple emission reception. Consequently, a hybrid sequence was chosen to optimize the frame rate while maintaining a sufficient angular diversity for the acquisition:

1) Three cylindrical waves were emitted sequentially from the entire probe and had to be repeated four times to record the reflected wavefront on each panel.

2) Two spherical waves (virtual source) were decomposed by panels, corresponding to 10 emissions.

The full ULM sequence thus corresponds to 32 emissions to achieve a volume rate of 209 Hz (*42*, *68*). Since only a few insonifications are used, the ULM acquisition consists of a partial reflection matrix that is acquired at multiple times t_{m} so that the reflected wavefronts are stored in a second matrix $\mathbf{R}' = \left[R'\left(\mathbf{u}_{\text{out}}, \mathbf{s}_{\text{in}}, \boldsymbol{\tau}, t_m\right)\right]$. The sparse feature of the recorded reflection matrices implies an ultrasound image of lower quality compared to a full measurement of the **R**-matrix. Both the contrast and, to a lesser extent, the resolution of the beamformed image are degraded. However, those detrimental effects are compensated, at least partially, by the echogenicity of the bubbles for the contrast and by the localization feature that allows the resolution to be no longer limited by diffraction but by the SNR (*15*). During this acquisition, microbubble injection boluses (SonoVue, Bracco, Italy) were injected, i.e., from 1.5 to 2 ml/min for 2.5 to 6.5 min.

A total of one to six acquisitions were performed per sheep. The experimental conditions are summarized in table S1. The raw ULM data used in the paper correspond to the ULM data presented in (*42*). It should also be noted that, for some acquisition, the UMI sequence is performed after the ULM sequence and not before, but this does not change the principle of the method.

Focused reflection matrix

A general procedure to build each focused reflection matrix, noted $\mathbf{R}_{\boldsymbol{\rho\rho}}(z)$, is to use a delay-and-sum (DAS) algorithm, which consists of applying appropriate time delays to create a double synthetic focusing procedure at both input and output (*57*). Mathematically, such a beamforming procedure is described by Eq. 1. The input and output times of flight, τ_{in} and τ_{out}, are given by

$$\tau_{\text{in/out}}(\mathbf{w}, \mathbf{r}) = \frac{|\mathbf{w} - \mathbf{r}|}{c_0} = \frac{\sqrt{\left(x - w_x\right)^2 + \left(y - w_y\right)^2 + \left(z - w_z\right)^2}}{c_0} \tag{4}$$

with $\mathbf{w} = \mathbf{v}_{\text{in}}$ at input and $\mathbf{w} = \mathbf{u}_{\text{out}}$ at output.

The confocal volume shown in Fig. 4A can be extracted from the diagonal elements of the reflection matrix ($\boldsymbol{\rho}_{\text{in}} = \boldsymbol{\rho}_{\text{out}}$), so that

$$\mathcal{I}(\boldsymbol{\rho}, z) = |R(\boldsymbol{\rho}, \boldsymbol{\rho}, z)|^2 \tag{5}$$

Reflection PSF

The off-diagonal points in $\mathbf{R}_{\boldsymbol{\rho\rho}}(z)$ can be exploited for a quantification of the focusing quality at any pixel of the ultrasound image. To that aim, the spreading of energy is investigated along each antidiagonal of $\mathbf{R}_{\boldsymbol{\rho\rho}}(z)$. Mathematically, this can be done by means of a change of variable to express the focused **R**-matrix in a common midpoint basis (*57*)

$$R\left(\Delta\boldsymbol{\rho}, \boldsymbol{\rho}_{\text{m}}, z\right) = R\left(\boldsymbol{\rho}_{\text{out}}, \boldsymbol{\rho}_{\text{in}}, z\right) \tag{6}$$

with $\boldsymbol{\rho}_{\text{m}} = \left(\boldsymbol{\rho}_{\text{in}} + \boldsymbol{\rho}_{\text{out}}\right)/2$ as the midpoint between $\boldsymbol{\rho}_{\text{in}}$ and $\boldsymbol{\rho}_{\text{out}}$ and $\Delta\boldsymbol{\rho} = \boldsymbol{\rho}_{\text{out}} - \boldsymbol{\rho}_{\text{in}}$ as their relative position. A local average of the backscattered intensity is then performed to smooth out the speckle reflectivity and provide an estimator of the RPSF

$$\text{RPSF}\left(\Delta\boldsymbol{\rho}, \mathbf{r}_{\text{p}}\right) = \left\langle |R\left(\Delta\boldsymbol{\rho}, \boldsymbol{\rho}_{\text{m}}, z\right)|^2 \mathcal{P}\left(\boldsymbol{\rho}_{\text{m}} - \boldsymbol{\rho}_{\text{p}}, z - z_{\text{p}}\right)\right\rangle_{\boldsymbol{\rho}_{\text{m}}, z} \tag{7}$$

with $\mathbf{r}_{\text{p}} = \left(\boldsymbol{\rho}_{\text{p}}, z_{\text{p}}\right)$. The symbol $\langle\cdots\rangle$ denotes a spatial average over the variables in the subscript. $\mathcal{P}\left(\boldsymbol{\rho}_{\text{m}} - \boldsymbol{\rho}_{\text{p}}, z - z_{\text{p}}\right) = 1$ for $|\boldsymbol{\rho}_{\text{m}} - \boldsymbol{\rho}_{\text{p}}| < p_{\rho}/2$ and $|z_{\text{m}} - z_{\text{p}}| < p_z/2$, and zero otherwise. The dimensions of $\mathcal{P}$ used for Figs. 3 (E to H) and 4 (C and D) are $\mathbf{p} = \left(p_{\rho}, p_z\right) = (4.3, 3)$ mm.

As shown in Figs. 3 (E to H) and 4 (C and D), the RPSF displays the following typical shape: a distorted confocal spot associated with singly scattered echoes on top of a flat background induced by multiple scattering events. On one hand, the extension $\delta\rho$ of the confocal peak is directly related to the local resolution of the ultrasound image. $\delta\rho$ can be obtained by considering the descanned

area $\mathcal{A}_{-3\mathrm{dB}}$ over which the normalized RPSF is larger than −3 dB (fig. S4), such that

$$\delta\rho = \sqrt{\mathcal{A}_{-3\mathrm{dB}}/\pi} \tag{8}$$

On the other hand, the multiple scattering rate α_M can be estimated by averaging the RPSF beyond the confocal peak, i.e., for $4\delta\rho_0 < \|\Delta\boldsymbol{\rho}\| < 6\delta\rho_0$

$$\alpha_M(\mathbf{r}_p) = \frac{\left\langle \mathrm{RPSF}(\Delta\boldsymbol{\rho}, \mathbf{r}_p)\right\rangle_{4\delta\rho_0<\|\Delta\boldsymbol{\rho}\|<6\delta\rho_0}}{\mathrm{RPSF}(\Delta\boldsymbol{\rho}=\mathbf{0}, \mathbf{r}_p)} \tag{9}$$

Aberration phase law

An aberration law is extracted using the distortion matrix framework (*57*, *62*) following these different steps:

1) We first project $\mathbf{R}_{\boldsymbol{\rho\rho}}(z)$ onto the transducer basis ($\mathbf{u}$) either at input or output using a homogeneous propagation model

$$\mathbf{R}_{\mathbf{u\rho}}(z) = \mathbf{T}_0(z) \times \mathbf{R}_{\boldsymbol{\rho\rho}}(z) \tag{10}$$

and

$$\mathbf{R}_{\boldsymbol{\rho u}}(z) = \mathbf{R}_{\boldsymbol{\rho\rho}}(z) \times \mathbf{T}_0^{\top}(\mathbf{z}) \tag{11}$$

where the upperscrit ⊤ stands for the matrix transpose, $\mathbf{T}_0 = [T_0(\mathbf{u}, \boldsymbol{\rho}, z)]$ is the transmission matrix between the probe and the set of voxels at depth z for an ideal homogeneous medium

$$T_0(\mathbf{u}, \boldsymbol{\rho}, z) = \frac{z\exp\left(jk_0\sqrt{\|\mathbf{u}-\boldsymbol{\rho}\|^2+z^2}\right)}{4\pi\left(\|\mathbf{u}-\boldsymbol{\rho}\|^2+z^2\right)} \tag{12}$$

As sketched in Fig. 2B, this dual reflection matrix contains the wavefronts associated with virtual sources corresponding to the focusing points $(\boldsymbol{\rho}_{\mathrm{in/out}}, z)$. Those wavefronts correspond to the sum of a geometric parabolic component related to the position of each focusing point $(\boldsymbol{\rho}_{\mathrm{in/out}}, z)$ and of a distorted component resulting from the mismatch between the propagation model and the real speed-of-sound distribution. This distorted component displays strong correlations because each reflected wavefront goes through the same part of the skull, the probe being placed at the skull surface. This is the so-called angular (or tilt-tilt) memory effect (*83*) that we will exploit in the following.

1) To do so, we isolate the distorted part of each wavefront by subtracting the geometric component that would be ideally obtained in the absence of aberrations (i.e., constant speed of sound c_0). The result is the input and output distortion matrices, which are expressed as follows

$$\mathbf{D}_{\mathbf{u\rho}}(z) = \mathbf{R}_{\mathbf{u\rho}}(z) \circ \overline{\mathbf{T}}_0^{*} \tag{13}$$

and

$$\mathbf{D}_{\boldsymbol{\rho u}}(z) = \mathbf{R}_{\boldsymbol{\rho u}}(z) \circ \overline{\mathbf{T}}_0^{\dagger} \tag{14}$$

where the symbols, ∘, * and † stand for the Hadamard (element-wise) product, matrix conjugate and conjugate transpose, respectively. $\overline{\mathbf{T}}_0$ is the normalized transmission matrix such that

$$\overline{T}_0(\mathbf{u}, \boldsymbol{\rho}, z) = T_0(\mathbf{u}, \boldsymbol{\rho}, z) / \left|T_0(\mathbf{u}, \boldsymbol{\rho}, z)\right|$$

In the focused basis, the operation described in Eq. 14 amounts to a descan of each virtual source $(\boldsymbol{\rho}_{\mathrm{in/out}}, z)$ at the origin $(\mathbf{0}, z)$ of each focal plane, as sketched in Fig. 2C. In the transducer basis, it consists of a realignment of associated wavefronts, thereby highlighting the angular correlations between wave distortions.

1) We then exploit this angular memory effect by computing the correlation matrices of wavefront distortions

$$\mathbf{C}_{\mathrm{in}}(z) = \mathbf{D}_{\mathbf{u\rho}}(z) \times \mathbf{D}_{\mathbf{u\rho}}^{\dagger}(z) \tag{15}$$

and

$$\mathbf{C}_{\mathrm{out}}(z) = \mathbf{D}_{\boldsymbol{\rho u}}^{\top}(z) \times \mathbf{D}_{\boldsymbol{\rho u}}^{*}(z) \tag{16}$$

2) A numerical IPR algorithm (*57*) is performed to extract an estimation of aberration laws $\Phi_{\mathrm{in/out}}(z) = \left[\phi_{\mathrm{in/out}}(\mathbf{u}_{\mathrm{in/out}}, z)\right]$ by solving the following equation

$$\Phi_{\mathrm{in/out}}(z) = \arg\left\{\mathbf{C}_{\mathrm{in/out}} \times \exp\left[i\Phi_{\mathrm{in/out}}(z)\right]\right\} \tag{17}$$

The IPR process, sketched in Fig. 2D, allows the synthesis of a coherent guide star from the set of virtual sources $(\boldsymbol{\rho}_{\mathrm{in/out}}, z)$. The associated wavefront is the resulting aberration phase law $\Phi_{\mathrm{out/in}}(z)$. The complexity of each aberration law can be quantified by the Strehl ratio, which is defined as follows (*67*) (see also section S3)

$$\mathcal{S}(z) = \left|\left\langle \exp\left[i\phi(\mathbf{u}, z)\right]\right\rangle_{\mathbf{u}}\right|^2 \tag{18}$$

The aberration phase laws yield an estimator of the input/output transmission matrix between the probe and each focal plane

$$\mathbf{T}_{\mathrm{in/out}}(z) = \exp\left(i\Phi_{\mathrm{out}}\right) \circ \mathbf{T}_0 \tag{19}$$

1) Aberrations are compensated by applying the phase conjugate of the transmission matrices to provide an updated focused reflection matrix

$$\mathbf{R}_{\boldsymbol{\rho\rho}}(z) = \mathbf{T}_{\mathrm{in}}^{\dagger}(z) \times \mathbf{R}_{\mathbf{u\rho}}(z) \tag{20}$$

and

$$\mathbf{R}_{\boldsymbol{\rho\rho}}(z) = \mathbf{R}_{\boldsymbol{\rho u}}(z) \times \mathbf{T}_{\mathrm{out}}^{*}(z) \tag{21}$$

The whole process is repeated two times at input and output to gradually improve the focusing process. The whole UMI process is summarized by the flow chart displayed in fig. S2. The confocal volume (Eq. 5) displayed in Fig. 4E and the map of RPSFs (Eq. 7) shown in Fig. 4D are extracted from the diagonal coefficients of this corrected focused reflection matrix.

Ultrasound localization microscopy

From the reflection matrix $\mathbf{R}'$ recorded using the hybrid sequence, a ULM image can be built by performing the following postprocessing steps.

1) High volume rate ultrasound images are constructed using a conventional DAS algorithm into a 30 mm–by–30 mm–by–60 mm volume with 0.5 mm–by–0.5 mm–by–0.5 mm voxels (*68*)

$$\mathcal{I}'(\boldsymbol{\rho}, z, t_m) = \sum_{\mathbf{s}_{\mathrm{in}}} \sum_{\mathbf{u}_{\mathrm{out}}} R'\left(\mathbf{u}_{\mathrm{out}}, \mathbf{s}_{\mathrm{in}}, \tau_{\mathrm{in}}(\mathbf{s}_{\mathrm{in}}, \boldsymbol{\rho}, z) + \tau_{\mathrm{out}}(\mathbf{u}_{\mathrm{out}}, \boldsymbol{\rho}, z), t_m\right)$$

2) A high-pass time filter is applied to the set of images by means of a two-frame sliding average window

$$\mathcal{I}''(\boldsymbol{\rho}, z, t_m) = \mathcal{I}'(\boldsymbol{\rho}, z, t_m) - \left\langle \mathcal{I}'(\boldsymbol{\rho}, z, t_n) \right\rangle_{n\in[m-1;m+1]}$$

Albeit crude, this simple operation allows the removal of most of the slow-varying component of the ultrasound image (i.e., tissues) while enhancing the dynamic part of the image (moving microbubbles).

1) The microbubbles were then detected in each volume by localizing regional maxima on each image $\mathcal{I}''$. The center of each PSF was sublocalized using the radial symmetry method (*84*–*86*), i.e., by assuming a Gaussian shape for the PSF and by applying a gradient algorithm. Microbubbles with an SNR below 10.5 dB were discarded. This SNR was calculated as the intensity at the center of the microbubbles divided by the mean intensity of the neighboring voxels over a 5-mm-wide patch. The detected bubbles and their localization are superimposed to one cross section of the ultrasound image in Fig. 5 (A and B).

2) Tracking algorithm has been performed using the Hungarian method (*87*) to build the histogram displayed in Fig. 5D. A maximum linking distance between two microbubbles is fixed to 1.5 mm. A one-frame gap is allowed, and no restriction on track duration is imposed.

3) A 3D ULM density map $\mathcal{U}(\mathbf{r})$ is obtained by accumulating and projecting all tracks of microbubbles onto a 3D grid whose spatial sampling is λ/10. The result is displayed in Fig. 6 (A and C).

The same process is applied to the ultrasound images $\mathcal{I}''$ corrected by UMI (Eq. 2). The resulting ULM maps are displayed in Fig. 6 (B and D).

Computational insights

The computation time of the UMI process (*57*) is limited by the beamforming of the focused **R**-matrix (Eq. 1) that takes 30 min here [on graphics processing unit (GPU) with CUDA language], while the aberration correction process only lasts for a few minutes. All the postprocessing was realized with MATLAB (R2024a) on a working station with two processors at 2.20 GHz and 128 GB of random-access memory and a GPU with 48 Go of dedicated memory. This computation time for UMI remains acceptable compared to the ULM process that takes 1 hour and 30 min for 9000 frames. It should be noted that the UMI process (beamforming and correction) can be further sped up by reducing the number of focusing points required to extract the aberration laws.

Angiographic MRI sequences

MRAs were performed with a 3T MRI scanner (GE SIGNA Premier) in a thermoregulated room, i.e., at ~20°C (axial propeller, repetition time = 5539 ms, time to echo = 165.744 ms, slice thickness = 2 mm, 31 slices, in-place resolution = 0.375 × 0.375). The superimposition of MRA and ULM images in Fig. 7 has been performed manually using Amira software (v2019.4, Thermo Fisher Scientific).

Supplementary Materials

The PDF file includes:

Sections S1 to S8
Figs. S1 to S9
Table S1
Legends for movies S1 and S2
References

Other Supplementary Material for this manuscript includes the following:

Movies S1 and S2

REFERENCES AND NOTES

1. M. Bahrami, M. Keyhanifard, M. Afzali, Spontaneous intracerebral hemorrhage, initial computed tomography (CT) scan findings, clinical manifestations and possible risk factors. *Am. J. Nucl. Med. Mol. Imaging* **22**, 106–112 (2022).
2. L. Scheldeman, A. Wouters, F. Boutitie, P. Dupont, S. Christensen, B. Cheng, M. Ebinger, M. Endres, J. B. Fiebach, C. Gerloff, K. W. Muir, N. Nighoghossian, S. Pedraza, C. Z. Simonsen, V. Thijs, G. Thomalla, R. Lemmens, WAKE-UP Investigators, Different mismatch concepts for magnetic resonance imaging-guided thrombolysis in unknown onset stroke. *Ann. Neurol.* **87**, 931–938 (2020).
3. J. D. Kirsch, M. Mathur, M. H. Johnson, G. Gowthaman, L. M. Scoutt, Advances in transcranial Doppler US: Imaging ahead. *Radiographics* **33**, E1–E14 (2013).
4. M. Versluis, E. Stride, G. Lajoinie, B. Dollet, T. Segers, Ultrasound contrast agent modeling: A review. *Ultrasound Med. Biol.* **46**, 2117–2144 (2020).
5. A. Tarighatnia, M. R. Fouladi, N. D. Nader, A. Aghanejad, H. Ghadiri, Recent trends of contrast agents in ultrasound imaging: A review of the classifications and applications. *Mater. Adv.* **3**, 3726–3741 (2022).
6. H.-L. Liu, C.-H. Fan, C.-Y. Ting, C.-K. Yeh, Combining microbubbles and ultrasound for drug delivery to brain tumors: Current progress and overview. *Theranostics* **4**, 432–444 (2014).
7. O. Couture, S. Bannouf, G. Montaldo, J.-F. Aubry, M. Fink, M. Tanter, Ultrafast imaging of ultrasound contrast agents. *Ultrasound Med. Biol.* **35**, 1908–1916 (2009).
8. O. Couture, M. Fink, M. Tanter, Ultrasound contrast plane wave imaging. *IEEE Trans. Ultrason. Ferroelectr. Freq. Control* **59**, 2676–2683 (2012).
9. C. Errico, J. Pierre, S. Pezet, Y. Desailly, Z. Lenkei, O. Couture, M. Tanter, Ultrafast ultrasound localization microscopy for deep super-resolution vascular imaging. *Nature* **527**, 499–502 (2015).
10. O. Couture, V. Hingot, B. Heiles, P. Muleki-Seya, M. Tanter, Ultrasound localization microscopy and super-resolution: A state of the art. *IEEE Trans. Ultrason. Ferroelectr. Freq. Control* **65**, 1304–1320 (2018).
11. K. Christensen-Jeffries, O. Couture, P. A. Dayton, Y. C. Eldar, K. Hynynen, F. Kiessling, M. O'Reilly, G. F. Pinton, G. Schmitz, M.-X. Tang, M. Tanter, R. J. G. van Sloun, Super-resolution ultrasound imaging. *Ultrasound Med. Biol.* **46**, 865–891 (2020).
12. P. Song, J. M. Rubin, M. R. Lowerison, Super-resolution ultrasound microvascular imaging: Is it ready for clinical use? *Z. Med. Phys.* **33**, 309–323 (2023).
13. E. Betzig, G. H. Patterson, R. Sougrat, O. W. Lindwasser, S. Olenych, J. S. Bonifacino, M. W. Davidson, J. Lippincott-Schwartz, H. F. Hess, Imaging intracellular fluorescent proteins at nanometer resolution. *Science* **313**, 1642–1645 (2006).
14. M. J. Rust, M. Bates, X. Zhuang, Sub-diffraction-limit imaging by stochastic optical reconstruction microscopy (STORM). *Nat. Methods* **3**, 793–796 (2006).
15. Y. Desailly, J. Pierre, O. Couture, M. Tanter, Resolution limits of ultrafast ultrasound localization microscopy. *Phys. Med. Biol.* **60**, 8723–8740 (2015).
16. V. Hingot, C. Errico, M. Tanter, O. Couture, Subwavelength motion-correction for ultrafast ultrasound localization microscopy. *Ultrasonics* **77**, 17–21 (2017).
17. M. R. Lowerison, N. V. C. Sekaran, W. Zhang, Z. Dong, X. Chen, D. A. Llano, P. Song, Aging-related cerebral microvascular changes visualized using ultrasound localization microscopy in the living mouse. *Sci. Rep.* **12**, 619 (2022).
18. J. Claron, V. Hingot, I. Rivals, L. Rahal, O. Couture, T. Deffieux, M. Tanter, S. Pezet, Large-scale functional ultrasound imaging of the spinal cord reveals in-depth spatiotemporal responses of spinal nociceptive circuits in both normal and inflammatory states. *Pain* **162**, 1047–1059 (2021).
19. O. Demeulenaere, Z. Sandoval, P. Mateo, A. Dizeux, O. Villemain, R. Gallet, B. Ghaleh, T. Deffieux, C. Deméné, M. Tanter, C. Papadacci, M. Pernot, Coronary flow assessment using 3-Dimensional ultrafast ultrasound localization microscopy. *JACC Cardiovasc. Imaging* **15**, 1193–1208 (2022).
20. K. B. Hansen, C. A. Villagómez-Hoyos, J. C. Brasen, K. Diamantis, V. Sboros, C. M. Sørensen, J. A. Jensen, in *2016 IEEE International Ultrasonics Symposium (IUS)* (IEEE, 2016), pp. 1–4.
21. I. Taghavi, S. B. Andersen, C. A. Villagomez Hoyos, M. B. Nielsen, C. M. Sorensen, J. A. Jensen, In vivo motion correction in super-resolution imaging of rat kidneys. *IEEE Trans. Ultrason. Ferroelectr. Freq. Control* **68**, 3082–3093 (2021).
22. J. Zhu, E. M. Rowland, S. Harput, K. Riemer, C. H. Leow, B. Clark, K. Cox, A. Lim, K. Christensen-Jeffries, G. Zhang, J. Brown, C. Dunsby, R. J. Eckersley, P. D. Weinberg, M.-X. Tang, 3D super-resolution US imaging of rabbit lymph node vasculature in vivo by using microbubbles. *Radiology* **291**, 642–650 (2019).
23. F. Lin, S. E. Shelton, D. Espíndola, J. D. Rojas, G. Pinton, P. A. Dayton, 3-D ultrasound localization microscopy for identifying microvascular morphology features of tumor

angiogenesis at a resolution beyond the diffraction limit of conventional ultrasound. *Theranostics* **7**, 196–204 (2017).
24. T. Opacic, S. Dencks, B. Theek, M. Piepenbrock, D. Ackermann, A. Rix, T. Lammers, E. Stickeler, S. Delorme, G. Schmitz, F. Kiessling, Motion model ultrasound localization microscopy for preclinical and clinical multiparametric tumor characterization. *Nat. Commun.* **9**, 1527 (2018).
25. C. Huang, W. Zhang, P. Gong, U.-W. Lok, S. Tang, T. Yin, X. Zhang, L. Zhu, M. Sang, P. Song, R. Zheng, S. Chen, Super-resolution ultrasound localization microscopy based on a high frame-rate clinical ultrasound scanner: An in-human feasibility study. *Phys. Med. Biol.* **66**, 08NT01 (2021).
26. C. Demené, J. Robin, A. Dizeux, B. Heiles, M. Pernot, M. Tanter, F. Perren, Transcranial ultrafast ultrasound localization microscopy of brain vasculature in patients. *Nat. Biomed. Eng.* **5**, 219–228 (2021).
27. L. Denis, S. Bodard, V. Hingot, A. Chavignon, J. Battaglia, G. Renault, F. Lager, A. Aissani, O. Hélénon, J.-M. Correas, O. Couture, Sensing ultrasound localization microscopy for the visualization of glomeruli in living rats and humans. *EBioMedicine* **91**, 104578 (2023).
28. S. Bodard, L. Denis, V. Hingot, A. Chavignon, O. Hélénon, D. Anglicheau, O. Couture, J.-M. Correas, Ultrasound localization microscopy of the human kidney allograft on a clinical ultrasound scanner. *Kidney Int.* **103**, 930–935 (2023).
29. S. Bodard, L. Denis, G. Chabouh, J. Battaglia, D. Anglicheau, O. Hélénon, J.-M. Correas, O. Couture, Visualization of renal glomeruli in human native kidneys with sensing ultrasound localization microscopy. *Invest. Radiol.* **59**, 561–568 (2024).
30. F. Knieling, S. Schmarz, L. Denis, E. Nedoschill, A. Buehler, V. Danko, H. Mandelbaum, F. B. Nuñez, N. Dürr, M. Schlunz-Hendann, F. Brassel, U. Felderhoff-Müser, J. Wölfle, J. Jüngert, C. Dohna-Schwake, N. Bruns, A. Regensburger, O. Couture, H. Reutter, A. Hilger, Ultrasound super-resolution imaging of neonatal cerebral vascular reorganization during neurovascular interventions. *Adv. Sci.* **12**, 2415235 (2025).
31. J. Yan, B. Huang, J. Tonko, M. Toulemonde, J. Hansen-Shearer, Q. Tan, K. Riemer, K. Ntagiantas, R. A. Chowdhury, P. D. Lambiase, R. Senior, M.-X. Tang, Transthoracic ultrasound localization microscopy of myocardial vasculature in patients. *Nat. Biomed. Eng.* **8**, 689–700 (2024).
32. L. Denis, E. Meseguer, A. Gaudemer, G. Jaklh, S. Bodard, G. Chabouh, D. Hervé, E. Vicaut, P. Amarenco, O. Couture, Transcranial ultrasound localization microscopy in moya moya patients using a clinical ultrasound system. *Theranostics* **15**, 4074–4083 (2024).
33. D. E. Soulioti, D. Espindola, P. A. Dayton, G. F. Pinton, Super-resolution imaging through the human skull. *IEEE Trans. Ultrason. Ferroelectr. Freq. Control* **67**, 25–36 (2020).
34. J. Robin, C. Demené, B. Heiles, V. Blanvillain, L. Puke, F. Perren, M. Tanter, In vivo adaptive focusing for clinical contrast-enhanced transcranial ultrasound imaging in human. *Phys. Med. Biol.* **68**, 025019 (2023).
35. B. Heiles, M. Correia, V. Hingot, M. Pernot, J. Provost, M. Tanter, O. Couture, Ultrafast 3D ultrasound localization microscopy using a 32 × 32 matrix array. *IEEE Trans. Med. Imaging* **38**, 2005–2015 (2019).
36. A. Chavignon, V. Hingot, C. Orset, D. Vivien, O. Couture, 3D transcranial ultrasound localization microscopy for discrimination between ischemic and hemorrhagic stroke in early phase. *Sci. Rep.* **12**, 14607 (2022).
37. O. Demeulenaere, A. Bertolo, S. Pezet, N. Ialy-Radio, B. Osmanski, C. Papadacci, M. Tanter, T. Deffieux, M. Pernot, In vivo whole brain microvascular imaging in mice using transcranial 3D ultrasound localization microscopy. *EBioMedicine* **79**, 103995 (2022).
38. J. R. McCall, R. DeRuiter, M. Ross, F. Santibanez, S. D. Hingtgen, G. F. Pinton, P. A. Dayton, Longitudinal 3-D visualization of microvascular disruption and perfusion changes in mice during the evolution of glioblastoma using super-resolution ultrasound. *IEEE Trans. Ultrason. Ferroelectr. Freq. Control* **70**, 1401–1416 (2023).
39. C. Bourquin, J. Porée, B. Rauby, V. Perrot, N. Ghigo, H. Belgharbi, S. Bélanger, G. Ramos-Palacios, N. Cortes, H. Ladret, L. Ikan, C. Casanova, F. Lesage, J. Provost, Quantitative pulsatility measurements using 3D dynamic ultrasound localization microscopy. *Phys. Med. Biol.* **69**, 045017 (2024).
40. S. Lei, C. Zhang, B. Zhu, Z. Gao, Q. Zhang, J. Liu, Y. Li, H. Zheng, T. Ma, In vivo ocular microvasculature imaging in rabbits with 3D ultrasound localization microscopy. *Ultrasonics* **133**, 107022 (2023).
41. L. Wei, G. Wahyulaksana, M. te Lintel Hekkert, R. Beurskens, E. Boni, A. Ramalli, E. Noothout, D. J. Duncker, P. Tortoli, A. F. W. van der Steen, N. de Jong, M. Verweij, H. J. Vos, High-frame-rate volumetric porcine renal vasculature imaging. *Ultrasound Med. Biol.* **49**, 2476–2482 (2023).
42. A. Coudert, L. Denis, A. Chavignon, S. Bodard, M. Naveau, P. P. Sistiaga, R. Saulnier, C. Orset, D. Vivien, C. Chappard, O. Couture, 3D transcranial ultrasound localization microscopy reveals major arteries in the sheep brain. *IEEE Trans. Ultrason. Ferroelectr. Freq. Control* **71**, 1666–1676 (2024).
43. P. Xing, V. Perrot, A. U. Dominguez-Vargas, S. Quessy, N. Dancause, J. Provost, 3D ultrasound localization microscopy of the nonhuman primate brain, *The Lancet* **111**, 105457 (2025).
44. G. Chabouh, L. Denis, S. Bodard, F. Lager, G. Renault, A. Chavignon, O. Couture, Whole organ volumetric sensing ultrasound localization microscopy for characterization of kidney structure. *IEEE Trans. Med. Imaging* **43**, 4055–4063 (2024).
45. P. Xing, J. Porée, B. Rauby, A. Malescot, E. Martineau, V. Perrot, R. L. Rungta, J. Provost, Phase aberration correction for in vivo ultrasound localization microscopy using a spatiotemporal complex-valued neural network. *IEEE Trans. Med. Imaging* **43**, 662–673 (2024).
46. H. W. Babcock, The possibility of compensating astronomical seeing. *Publ. Astron. Soc. Pac.* **65**, 229–236 (1953).
47. A. Labeyrie, Attainment of diffraction limited resolution in large telescopes by fourier analysing speckle patterns in star images. *Astron. Astrophys.* **6**, 85–87 (1970).
48. R. A. Muller, A. Buffington, Real-time correction of atmospherically degraded telescope images through image sharpening. *J. Opt. Soc. Am.* **64**, 1200–1210 (1974).
49. F. Roddier, Ed., *Adaptive Optics in Astronomy* (Cambridge Univ. Press, 2009).
50. M. Hirama, O. Ikeda, T. Sato, Adaptive ultrasonic array imaging system through an inhomogeneous layer. *J. Acoust. Soc. Am.* **71**, 100–109 (1982).
51. L. Nock, G. E. Trahey, S. W. Smith, Phase aberration correction in medical ultrasound using speckle brightness as a quality factor. *J. Acoust. Soc. Am.* **85**, 1819–1833 (1989).
52. S. Flax, M. O'Donnell, Phase-aberration correction using signals from point reflectors and diffuse scatterers: Basic principles. *IEEE Trans. Ultrason. Ferroelectr. Freq. Control* **35**, 758–767 (1988).
53. R. Mallart, M. Fink, Adaptive focusing in scattering media through sound-speed inhomogeneities: The van Cittert Zernike approach and focusing criterion. *J. Acoust. Soc. Am.* **96**, 3721–3732 (1994).
54. G. Montaldo, M. Tanter, M. Fink, Time reversal of speckle noise. *Phys. Rev. Lett.* **106**, 054301 (2011).
55. S.-E. Måsøy, T. Varslot, B. Angelsen, Iteration of transmit-beam aberration correction in medical ultrasound imaging. *J. Acoust. Soc. Am.* **117**, 450–461 (2005).
56. M. O'Donnell, S. Flax, Phase-aberration correction using signals from point reflectors and diffuse scatterers: Measurements. *IEEE Trans. Ultrason. Ferroelectr. Freq. Control* **35**, 768–774 (1988).
57. F. Bureau, J. Robin, A. Le Ber, W. Lambert, M. Fink, A. Aubry, Three-dimensional ultrasound matrix imaging. *Nat. Commun.* **14**, 6793 (2023).
58. T. Varslot, H. Krogstad, E. Mo, B. A. Angelsen, Eigenfunction analysis of stochastic backscatter for characterization of acoustic aberration in medical ultrasound imaging. *J. Acoust. Soc. Am.* **115**, 3068–3076 (2004).
59. J.-L. Robert, M. Fink, Green's function estimation in speckle using the decomposition of the time reversal operator: Application to aberration correction in medical imaging. *J. Acoust. Soc. Am.* **123**, 866–877 (2008).
60. A. Badon, V. Barolle, K. Irsch, A. C. Boccara, M. Fink, A. Aubry, Distortion matrix concept for deep optical imaging in scattering media. *Sci. Adv.* **6**, eaay7170 (2020).
61. W. Lambert, L. A. Cobus, M. Couade, M. Fink, A. Aubry, Reflection matrix approach for quantitative imaging of scattering media. *Phys. Rev. X* **10**, 021048 (2020).
62. W. Lambert, L. A. Cobus, T. Frappart, M. Fink, A. Aubry, Distortion matrix approach for ultrasound imaging of random scattering media. *Proc. Natl. Acad. Sci. U.S.A.* **117**, 14645–14656 (2020).
63. W. Lambert, J. Robin, L. A. Cobus, M. Fink, A. Aubry, Ultrasound matrix imaging–Part I: The focused reflection matrix, the F-factor and the role of multiple scattering. *IEEE Trans. Med. Imaging* **41**, 3907–3920 (2022).
64. F. J. Fry, J. E. Barger, Acoustical properties of the human skull. *J. Acoust. Soc. Am.* **63**, 1576–1590 (1978).
65. J. Provost, C. Papadacci, J. E. Arango, M. Imbault, M. Fink, J.-L. Gennisson, M. Tanter, M. Pernot, 3D ultrafast ultrasound imaging in vivo. *Phys. Med. Biol.* **59**, L1–L13 (2014).
66. W. Lambert, L. A. Cobus, J. Robin, M. Fink, A. Aubry, Ultrasound matrix imaging–Part II: The distortion matrix for aberration correction over multiple isoplanatic patches. *IEEE Trans. Med. Imaging* **41**, 3921–3938 (2022).
67. V. N. Mahajan, Strehl ratio for primary aberrations: Some analytical results for circular and annular pupils. *J. Opt. Soc. Am.* **72**, 1258 (1982).
68. A. Coudert, A. Chavignon, L. Denis, O. Couture, Volumetric ultrasound localization microscopy with diverging cylindrical waves. *IEEE Trans. Ultrason. Ferroelectr. Freq. Control* **71**, 1657–1665 (2024).
69. E. Kalsoum, X. Leclerc, A. Drizenko, J.-P. Pruvo, in *Encyclopedia of the Neurological Sciences* (Elsevier, 2014), pp. 803–805.
70. D.-Y. Tsai, Y. Lee, E. Matsuyama, Information entropy measure for evaluation of image quality. *J. Digit. Imaging* **21**, 338–347 (2007).
71. S. Boruah, G. R. Paskoff, B. S. Shender, D. L. Subit, R. S. Salzar, J. R. Crandall, Variation of bone layer thicknesses and trabecular volume fraction in the adult male human calvarium. *Bone* **77**, 120–134 (2015).
72. K. Adanty, K. N. Rabey, M. R. Doschak, K. B. Bhagavathula, J. D. Hogan, D. L. Romanyk, S. Adeeb, S. Ouellet, T. A. Plaisted, S. S. Satapathy, C. R. Dennison, Cortical and trabecular morphometric properties of the human calvarium. *Bone* **148**, 115931 (2021).
73. H. Bendjador, T. Deffieux, M. Tanter, The SVD beamformer: Physical principles and application to ultrafast adaptive ultrasound. *IEEE Trans. Med. Imaging* **39**, 3100–3112 (2020).
74. H. Bendjador, S. Décombas-Deschamps, M. Dioguardi Burgio, R. Sartoris, B. Van Beers, V. Vilgrain, T. Deffieux, M. Tanter, The SVD beamformer with diverging waves: A proof-of-concept for fast aberration correction. *Phys. Med. Biol.* **66**, 18LT01 (2021).

75. D. Zhao, L. N. Bohs, G. E. Trahey, Phase aberration correction using echo signals from moving targets I: Description and theory. *Ultrason. Imaging* **14**, 97–110 (1992).
76. B.-F. Osmanski, G. Montaldo, M. Tanter, M. Fink, Aberration correction by time reversal of moving speckle noise. *IEEE Trans. Ultrason. Ferroelectr. Freq. Control* **59**, 1575–1583 (2012).
77. P. Balondrade, V. Barolle, N. Guigui, E. Auriant, N. Rougier, C. Boccara, M. Fink, A. Aubry, Multi-spectral reflection matrix for ultrafast 3D label-free microscopy. *Nat. Photonics* **18**, 1097–1104 (2024).
78. E. Giraudat, A. Burtin, A. Le Ber, M. Fink, J.-C. Komorowski, A. Aubry, Matrix imaging as a tool for high-resolution monitoring of deep volcanic plumbing systems with seismic noise. *Commun. Earth Environ.* **5**, 509 (2024).
79. S. Park, Y. Jo, M. Kang, J. H. Hong, S. Ko, S. Kim, S. Park, H. C. Park, S.-H. Shim, W. Choi, Label-free adaptive optics single-molecule localization microscopy for whole zebrafish. *Nat. Commun.* **14**, 4185 (2023).
80. U. Nanni, F. Gimbert, P. Roux, A. Lecointre, Observing the subglacial hydrology network and its dynamics with a dense seismic array. *Proc. Nat. Acad. Sci. U.S.A.* **118**, e2023757118 (2021).
81. U. Nanni, P. Roux, F. Gimbert, A. Lecointre, Dynamic imaging of glacier structures at high-resolution using source localization with a dense seismic array. *Geophys. Res. Lett.* **49**, e2021GL095996 (2022).
82. M. Schneider, Characteristics of SonoVue. *Echocardiography* **16**, 743–746 (1999).
83. G. Osnabrugge, R. Horstmeyer, I. N. Papadopoulos, B. Judkewitz, I. M. Vellekoop, Generalized optical memory effect. *Optica* **4**, 886–892 (2017).
84. B. Heiles, A. Chavignon, A. Bergel, V. Hingot, H. Serroune, D. Maresca, S. Pezet, M. Pernot, M. Tanter, O. Couture, Volumetric ultrasound localization microscopy of the whole brain microvasculature. *IEEE Open J. Ultrason. Ferroelectr. Freq. Control* **2**, 261–282 (2022).
85. B. Heiles, A. Chavignon, V. Hingot, P. Lopez, E. Teston, O. Couture, Performance benchmarking of microbubble-localization algorithms for ultrasound localization microscopy. *Nat. Biomed. Eng.* **6**, 605–616 (2022).
86. R. Parthasarathy, Rapid, accurate particle tracking by calculation of radial symmetry centers. *Nat. Methods* **9**, 724–726 (2012).
87. J.-Y. Tinevez, simpletracker code (2019); https://github.com/tinevez/simpletracker.
88. M. Tanter, J.-L. Thomas, M. Fink, Time reversal and the inverse filter. *J. Acoust. Soc. Am.* **108**, 223–234 (2000).
89. L. Denis, E. Meseguer, A. Gaudemer, G. Jaklh, S. Bodard, G. Chabouh, D. Hervé, E. Vicaut, P. Amarenco, O. Couture, Transcranial ultrasound localization microscopy in moyamoya patients using a clinical ultrasound system. *Theranostics* **15**, 4074–4083 (2025).

Acknowledgments: We thank the laboratory Cyceron, Institut Blood and Brain (Normandie Université, INSERM), where the sheep experiments were initially performed. In particular, we thank M. Naveau, P. Pro-Sistiaga, R. Saulnier, C. Orset, and D. Vivien. We also thank C. Chappard for the micro-CT imaging. **Funding:** This project has received funding from the European Research Council (ERC) under the European Union's Horizon 2020 research and innovation program (grant agreement nos. 772786 and 610110, ResolveStroke and REMINISCENCE projects, to O.C. and A.A., respectively). **Author contributions:** O.C. contributed to the conception of the ULM study. A.A. initiated and supervised the UMI part of the project. A.C., F.B., and L.D. contributed to the conception of the ultrasound sequences. L.D. and A.C. contributed to data acquisition. F.B. performed the UMI analysis. L.D. and A.C. performed the ULM analysis. L.D., F.B., A.C., O.C., and A.A. contributed to the interpretation of the experimental data. F.B., L.D., A.C., and A.A. prepared the figures. F.B., L.D., and A.A. contributed to drafting the manuscript. F.B., L.D., A.C., M.F., O.C., and A.A. discussed the results and contributed to finalizing the manuscript. **Competing interests:** A.A. and M.F. are inventors on a patent related to UMI held by CNRS (no. US11346819B2, published May 2022). A.C. and O.C. are inventors on a patent related also held by CNRS (no. US20240041423A1, published August 2024). O.C. is a cofounder and shareholder of the startup ResolveStroke. The authors declare that they have no other competing interests. **Data and materials availability:** The ultrasound data generated in this study are available at Zenodo (https://zenodo.org/records/15344797). All data needed to evaluate the conclusions in the paper are present in the paper and/or the Supplementary Materials.

Submitted 18 October 2024
Accepted 1 July 2025
Published 30 July 2025
10.1126/sciadv.adt9778